



HAL
open science

Complexity of Fault Rupture and Fluid Leakage in Shale: Insights From a Controlled Fault Activation Experiment

Yves Guglielmi, Christophe Nussbaum, Pierre Jeanne, Jonny Rutqvist, Frédéric Cappa, Jens Birkholzer

► **To cite this version:**

Yves Guglielmi, Christophe Nussbaum, Pierre Jeanne, Jonny Rutqvist, Frédéric Cappa, et al.. Complexity of Fault Rupture and Fluid Leakage in Shale: Insights From a Controlled Fault Activation Experiment. *Journal of Geophysical Research: Solid Earth*, 2020, 125 (2), pp.e2019JB017781. 10.1029/2019JB017781 . hal-02484643

HAL Id: hal-02484643

<https://hal.science/hal-02484643>

Submitted on 19 Feb 2020

HAL is a multi-disciplinary open access archive for the deposit and dissemination of scientific research documents, whether they are published or not. The documents may come from teaching and research institutions in France or abroad, or from public or private research centers.

L'archive ouverte pluridisciplinaire **HAL**, est destinée au dépôt et à la diffusion de documents scientifiques de niveau recherche, publiés ou non, émanant des établissements d'enseignement et de recherche français ou étrangers, des laboratoires publics ou privés.

JGR Solid Earth

RESEARCH ARTICLE

10.1029/2019JB017781

Key Points:

- Stress controlled the initiation of fault reactivation during the fluid injection
- The fault geometrical complexities dominated rupture propagation that was characterized by a succession of slip and opening events along the fault
- A large fluid leakage event occurred when injection pressure got close to the fault normal stress (i.e., the clamping stress)

Supporting Information:

- Supporting Information S1
- Data Set S1
- Data Set S2

Correspondence to:

Y. Guglielmi,
yguglielmi@lbl.gov

Citation:





Guglielmi, Y., Nussbaum, C., Jeanne, P., Rutqvist, J., Cappa, F., & Birkholzer, J. (2020). Complexity of fault rupture and fluid leakage in shale: Insights from a controlled fault activation experiment. *Journal of Geophysical Research: Solid Earth*, 125, e2019JB017781. <https://doi.org/10.1029/2019JB017781>

Received 2 APR 2019

Accepted 11 DEC 2019

Accepted article online 30 JAN 2020

Complexity of Fault Rupture and Fluid Leakage in Shale: Insights From a Controlled Fault Activation Experiment

Yves Guglielmi¹ , Christophe Nussbaum², Pierre Jeanne¹ , Jonny Rutqvist¹ , Frédéric Cappa^{3,4} , and Jens Birkholzer¹

¹Lawrence Berkeley National Laboratory, Energy Geosciences Division, Berkeley, CA, USA, ²Federal Office of Topography, Wabern, Switzerland, ³Université Côte d'Azur, CNRS, Observatoire de la Côte d'Azur, IRD, Géozur, Nice, France, ⁴Institut Universitaire de France, Paris, France

Abstract We observed rupture growth caused by controlled fluid injections at 340-m depth within a fault zone in the low-permeability Opalinus Clay in the Mont Terri Underground Research Laboratory (Switzerland). The rupture mechanisms were evaluated using measurements of the three-component borehole wall displacements and fluid pressure in two sections of the fault zone and located horizontally 3 m apart from each other. One section was set across a secondary segment of the fault and used for stepwise fluid injection intended to trigger rupture growth. The other section was set across the principal shear zone of the fault for monitoring. After stepwise pressure increase up to 5.95 MPa at injection, rupture initiated as slip activation, followed by an overall opening of the fault planes connected to the injection. After 19 s of continued injection, displacements arrived at the monitoring point on the principal shear zone. These displacements are about 2.4 times larger than in the secondary fault segment. Overall, the displacements corresponded to a normal fault activation. About 9 s after the displacement front arrived, a strong pressure increase of 4.17 MPa was measured at the monitoring point, indicating a hydraulic connection had formed along the initially very low permeability fault planes between the injection and the monitoring points. Our analyses highlight that the fault activation is consistent with the state of stress but that injection pressure must be close to the normal stress acting on the fault for permeability to be generated and for fluid leakage to occur.

1. Introduction

Injection of fluids into the subsurface can generate large overpressures perturbing the long-term stresses stored in rocks, which could potentially induce seismicity and leakage along preexisting faults (Ellsworth, 2013; Raleigh et al., 1976; Savage et al., 2017). Generally, the stability of a fault and the related reactivation mechanisms are estimated using the theory of elastoplasticity, considering a Mohr-Coulomb rupture criterion and the conditions of plastic strain localization in the fault gouge (Rice, 1976). When applying this criterion, the stress state relative to the frictional strength limit is considered as the dominant factor of fault reactivation by fluid injection.

The common assumption is that faults critically oriented for shear reactivation are expected to be the most permeable (Barton et al., 1995). The faults are considered “critically stressed” when stresses calculated normal and tangential to their surface given the in situ stress field place them close to instability according to the Mohr-Coulomb rupture criterion. However, in many cases it appears that the relationship between the “critical stress” state of faults and their permeability is not straightforward (Evans, 2005; Matilla & Tammisto, 2012), and laboratory experiments have shown that fluid flow can occur in faults of any orientation (Cuss et al., 2015). In detail, Cuss et al. (2015) found that injected gas may enter a fault gouge zone both as a function of stress acting on the fault surface, and as a result of slight deformations of pore throat size that generate complex and nonrepeatable channeling in the fault gouge material (Cuss et al., 2015). Previously, during laboratory tests on fractures without filling, Barton et al. (1985) and Olsson and Barton (2001) demonstrated that the coupling between fracture shear displacement or normal closure and fracture hydraulic conductivity variations depended both on the stress conditions and on fracture surface characteristics such as the roughness. Recent laboratory results highlight that the variation in effective normal stress related to local fluid injection in a fault plane does not imply complete separation of the two sides of a fault because complex channeling effects may favor heterogeneous pore pressure variations within the fault plane

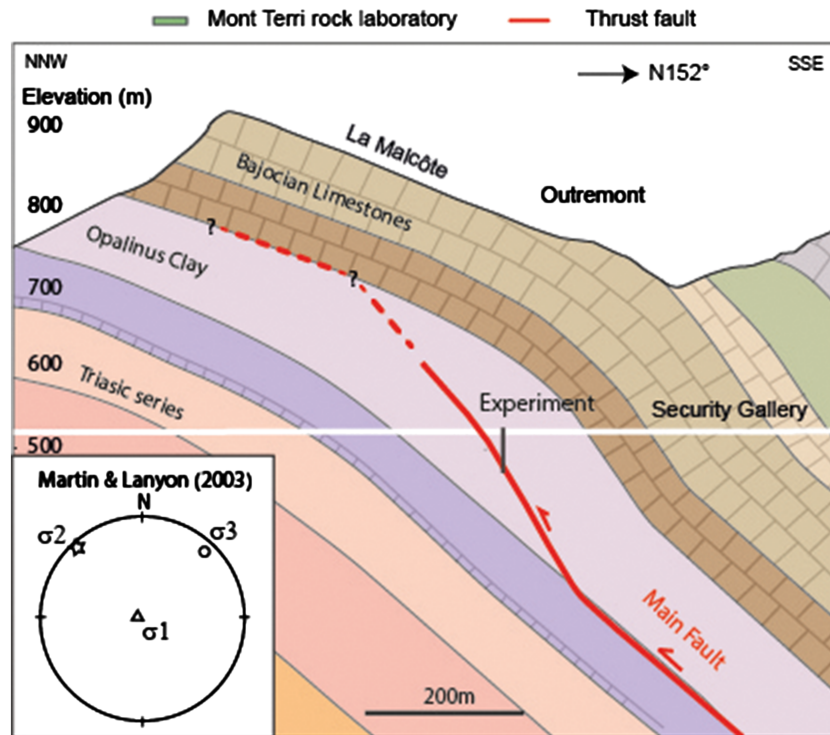


Figure 1. Geological cross section showing the Main Fault geometry and the experimental borehole location. Martin and Lanyon's tensor orientation (2003), which is considered the most comprehensive Mont Terri stress compilation to date, is plotted in the lower left corner.

controlling leakage and nonlocal rupture initiation before the Coulomb rupture criterion is exceeded (Passelègue et al., 2018).

These channeling effects observed along a single fracture or fault plane can become more pronounced within complex geometries of fault zones. Indeed, faults are rarely planar over length scales and often comprise a multicompartiment architecture that consists of multiple cores, where thin gouge layers may accommodate most of the strain, surrounded by densely fractured damage zones (Faulkner et al., 2003; Mitchell & Faulkner, 2009). These fracture zones are made up of subsidiary faults, some of them displaying significantly different orientations compared to the average orientation of the fault zone (Choi et al., 2016; Mitchell & Faulkner, 2009). Thus, fault geometrical complexities are visible at multiple scales. It is then reasonable to infer that some critically stressed subsidiary faults may exist in the fault zone, favoring local earthquake rupture nucleation and fluid leakage even if the main fault zone is less favorably oriented for shear reactivation (Townend & Zoback, 2000). In addition, damage-induced changes in elastic fault zone properties have been observed to induce local perturbations of the regional stress (Hearn & Fialko, 2009; Niu et al., 2008) which, as some researchers conclude, may favor fluid-assisted faulting process (Faulkner et al., 2006; Leclère et al., 2015).

Fault rupture associated with fluid pressures is well documented, but the mechanisms by which rupture in complex fault zones occurs remain unclear. Here, we analyze the evolution of rupture with fluid leakage through direct in situ measurements of three-dimensional displacements on fault structures in a shale formation (Opalinus Clay). Hydraulic injection tests were conducted at 340 m depth between packer-isolated intervals in two vertical boreholes across a ~10-m-thick mature fault zone in the Mont Terri underground research facility in Switzerland (Figure 1) (Thury & Bossart, 1999). The test intervals of the two boreholes were set in two contrasted fault facies, the first being in the fractured damage zone and the other one extending across the main slip plane of the fault zone. During injection into the first borehole (i.e., the injection borehole), a hydraulic connection associated with fault movement occurred between the two boreholes, which are separated 3 m horizontally (Figure 2). In both borehole intervals, we used a “SIMFIP”

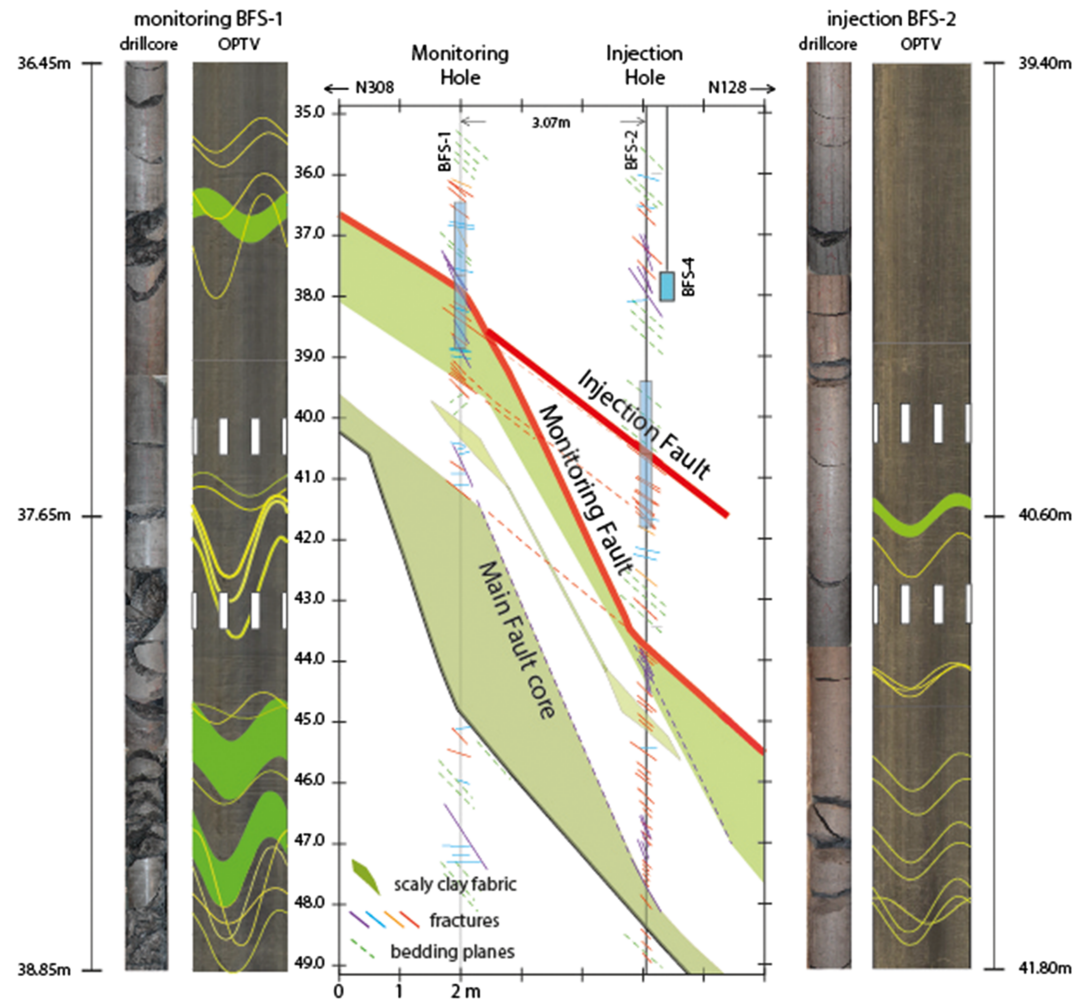


Figure 2. (middle) Vertical cross section of the structural setting of the Main Fault activation experiment (blue rectangles shows the location of the test intervals). (left and right) Cores and optical log of BFS-1 and BFS-2 intervals (white rectangles on the optical log show the exact location of the anchors of the displacement sensor).

instrument (Guglielmi et al., 2014), which is a three-component fiber optic extensometer that monitors borehole wall displacement during fluid pressurization of the interval.

In a previous paper (Jeanne et al., 2018), we used a numerical model with a simplified planar fault geometry to explore how a rate dependency of both fault friction and permeability could explain the onset of rupture observed in the injection borehole. The rupture occurred on a secondary fault located in the damage zone of the main fault (Jeanne et al., 2018). In the present paper, we present a complete experimental data set which includes new measurements of injection rate, pore pressure, and displacement variations observed at the monitoring hole, and we estimate the influence of the fault geometry on the observed displacement complexities and fluid pathways. We show that following rupture initiation at the injection hole, a hydraulic connection occurred between the two boreholes, characterized by a large flowrate increase and associated with a complex reactivation event in the main slip plane of the fault zone (referred to as the Main Fault Principal Shear Zone). Here, we investigate how the SIMFIP pressure and displacement signals can be used to estimate the transient evolution of fault slip and opening as a function of time and pressure increase. This is done through establishing a correlation between the measured displacement orientations and the characteristics of discontinuities observed via borehole optical logs in the packer-isolated intervals. We then explore how the displacements observed on the identified fault planes agree with the average Mont Terri stress tensor. Our analysis highlights that a large effective normal stress (i.e., the clamping stress) reduction was

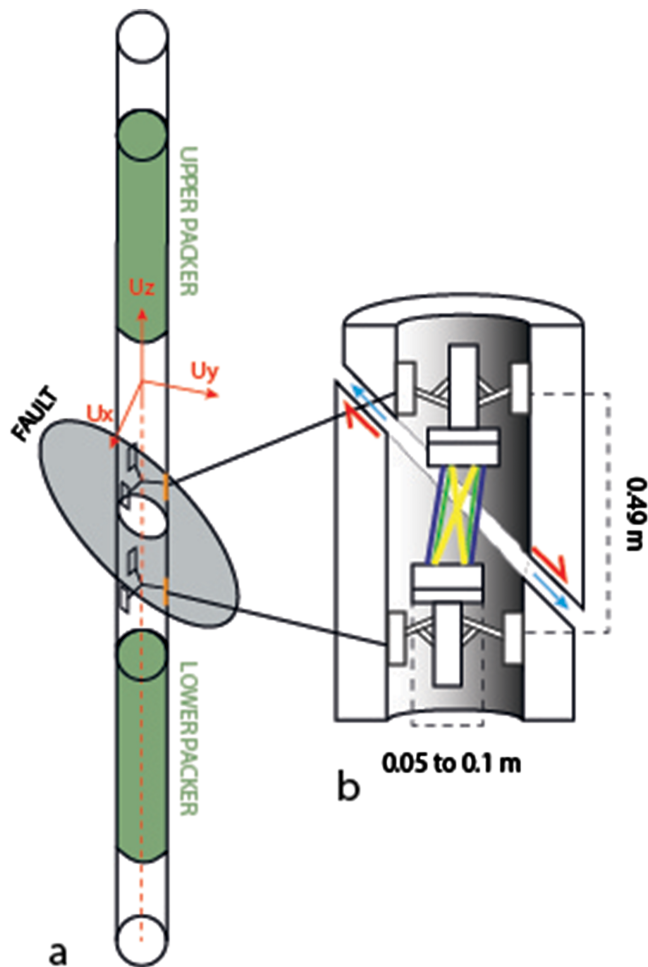


Figure 3. (a) SIMFIP straddle packer probe and (b) details of the instrument used to monitor fault displacements at both BFS-1 and BFS-2 intervals. The fault zones across which the SIMFIP sensor is set are named as the injection and the monitoring faults in Figure 2.

necessary to propagate the fault rupture and to cause a significant leakage event. In details, this propagation exhibits a very complex behavior in space and time. It is characterized by a transient evolution of combined opening and slip, with the displacement behavior observed in the secondary fault where injection occurred (also referred to as Injection Fault) being distinctly different from the behavior in the Principal Shear Zone of the Main Fault (also referred to as Monitoring Fault) (Figure 2). Finally, we discuss that invoking frictional slip on such a mature fault simplified as a single plane (or a thin layer) is not adequate when evaluating fault activation and associated leakage potential.

2. Tectonic Setting: Geological Structures, Stress Conditions, and Location of Injection Tests

The Mont Terri Underground Research Laboratory was built for the hydrogeological, geochemical, and geotechnical characterization of the Opalinus Clay formation, which is investigated as a potential host rock for deep geologic nuclear waste disposal in Switzerland. The Opalinus Clay is also quite representative of formations typically considered as caprock in the case of geological carbon dioxide (CO₂) storage in deep geological reservoirs (Goodman et al., 2017). The laboratory consists of multiple tunnels and galleries located in the SW-NE trending Mont Terri anticline, which is a flat-ramp-flat structure thrust toward the NW (fault-bend fold) and where the studied fault, although called the “Main Fault” because it is the most deformed zone intersected by the laboratory facilities, is a minor splay (third order structure; Figure 1). The Mont Terri Main Fault consists of a thrust zone, about 0.8 to 3 m width, bounded by two major fault planes. The upper fault boundary (also referred to as the Main Fault Principal Shear Zone) plane has a strike of N066° and a dip of 45°SE, whereas the lower fault boundary has a strike of N075° and a dip of 40°SE. At depth, the strike of those two main planes may vary from N050°-to-N075° and the dip from 40°-to-65°SE (Figure 1). The fracture network visible at the gallery walls and on borehole cores, and deformations within the Main Fault are heterogeneous (Nussbaum et al., 2011), including gouge, C'-type shear bands, folds, numerous fault planes cutting the fault zone from centimeter to meter scales and some “intact”

parts. The different sets of minor faults within the Main Fault structure correspond to Riedel P- and R-shears. Around that thrust core, there is a damaged zone of variable thickness and other secondary splay fault zones. The main fault cuts the bedding, which has a strike and dip of N055°-to-N065° and 50-to-55° SE, respectively. Thus, in some areas, the fault is almost parallel to the bedding, whereas in other areas there is an angle of 10° to 15° between the dip orientations of the main fault surface and the bedding.

The stress tensor has been estimated at different locations in the Mont Terri Laboratory through three different types of measurements: (1) with a Slotter probe utilizing a strain relief testing method; (2) based on the undercore method using the CSIRO triaxial strain cells (Wiles & Kaiser, 1994a, 1994ab); and (3) via hydraulic fracturing tests (Haimson & Fairhurst, 1970). The results from all these measurements are discussed in Martin and Lanyon (2003) and in Corkum and Martin (2007) who proposed the following “synthesized” value at the depth of the galleries in the Mont Terri underground research laboratory, characterized by the following total principal stresses: $\sigma_1 = 6\text{--}7$ MPa subvertical to N210–70°plunge, $\sigma_2 = 4\text{--}5$ MPa N320° subhorizontal to 7° plunge, and $\sigma_3 = 0.6\text{--}2.2$ MPa N052° subhorizontal to 18° plunge. The greatest uncertainty is the magnitude of σ_3 , which appears low compared to the pore pressure of about 2 MPa measured away from the excavation damage zone of the galleries. For these reasons, other authors recently reestimated σ_3 and reported higher values of 2.5-to-2.9 MPa (Amann et al., 2018). In addition, the hydraulic tests allowed for a good estimate of the stress magnitude normal to the bedding planes, estimated to be 4.2 MPa. Uncertainty ranges for the orientation of the principal stresses have not been clearly estimated. The slight

Table 1
Displacement Vectors Picked at the Injection and at the Monitoring Chambers

Event	Displacement vector	Start time (s)	End time (s)	Trend or azimuth (°)	Plunge (°)	Norm (10 ⁻⁶ m)	Activation pressure (MPa)	Activated plane and activation mode
Event 1	\vec{u}_1	6,668	7,533	318	-7	13	1.70	—
	$\vec{u}_{2.1}$	7,557	7,665	128	-8	4	1.95	—
	$\vec{u}_{2.2}$	7,690	7,823	126	-8	4	2.27	—
	$\vec{u}_{2.3}$	7,854	8,056	127	-5	5	2.61	—
	$\vec{u}_{2.4}$	8,086	8,211	135	-7	8	3.05	—
	\vec{u}_3	8,245	8,247	95	-26	96	3.45	Injection Fault normal faulting
Event 2	\vec{v}_1	14,204	14,322	296	13	102	2.41	—
	$\vec{v}_{2.1}$	14,350	14,420	153	10	5	3.69	—
	$\vec{v}_{2.2}$	14,457	14,510	168	12	3	4.04	—
	$\vec{v}_{2.3}$	14,532	14,590	135	15	4	4.54	—
	$\vec{v}_{2.4}$	14,612	14,750	143	2	14	5.00	—
Event 3	\vec{v}_{3i}	14,770	14,863	251	50	35	5.43	Injection Fault opening
	\vec{v}_{3m}	14,780	14,801	287	5	31	0.45	—
	\vec{v}_{4m}	14,850	14,863	217	-28	228	3.93	Monitoring fault zone normal faulting
	\vec{v}_{4i}	14,863	15,010	46	-57	27	4.26	—

Note. The most significant Events 1–3 are figured in red (Negative plunge = downward, Positive plunge = upward).

plunge of σ_1 and the low value of σ_3 could be related to a topographic effect due to a deep valley to the southwest of the Mont Terri site. Finally, most of the stress estimations were done at the gallery level. There is a limited (and unpublished) number of stress measurements at the depth of the experiment which is ~40 m below the galleries, which tend to show higher values up to 3.9 MPa for σ_3 (Doe & Vietor, 2015). Table 2 shows a summary of the range of values for the reference Mont Terri stress tensor.

In this geological context, the injection tests described in this study were conducted at 40.6 m depth below the main laboratory gallery (corresponding to 340.6-m depth below the topographic surface) in the vertical borehole (BFS-2) drilled from the gallery floor (Figure 2). A second vertical borehole (BFS-1) located 3.07 m horizontally from BFS-2 was used to monitor the fault core movement at a depth of 37.65 m below the gallery floor (Figure 2). The gallery cross section is about 4 m × 4 m and the excavation damage zone extends approximately 3 to 4 m from the gallery wall. Deformations around the gallery are impacted by a strong mechanical anisotropy induced by the bedding (Amann et al., 2017; Bock et al., 2010). Stress perturbations caused by the tunnel presence are estimated to increase to about +6 MPa and +2 MPa at the gallery wall, respectively, for σ_1 and σ_3 . These stress concentrations are vanishing at the limits of the excavation damage zone (Martin & Lanyon, 2003). Thus, the injection tests were conducted far enough from the influence of the gallery. Injection into BFS-2 occurred about one week after the boreholes were drilled, which was done with air as drilling fluid. At the end of the drilling, the boreholes were dry, the overall permeability of the rock being so low that no flow was detected. To prepare for the injection, only the interval between the two inflatable packers was initially saturated with water in chemical equilibrium with the formation. The borehole sections above and below the interval remained dry and at atmospheric pressure.

Initial pore pressures in the fault zone and in the intact rock were measured by three mini piezometers installed in slim boreholes as follows:

1. BFS4 was set 3 m horizontally from the fault core and 2 m from the injection chamber in the fault damage zone (Figure 2).
2. BFS6 was set ~2 m horizontally from the fault core and 8 m shallower than the injection chamber in the fault damage zone.
3. BFS5 was set 20 m horizontally from the fault zone in the intact rock.

Each minipiezometer comprised of a 20-mm diameter and 55-mm-long packer installed at a distance of 3 mm to the borehole end. The packer was mechanically fixed to the borehole wall and the remaining

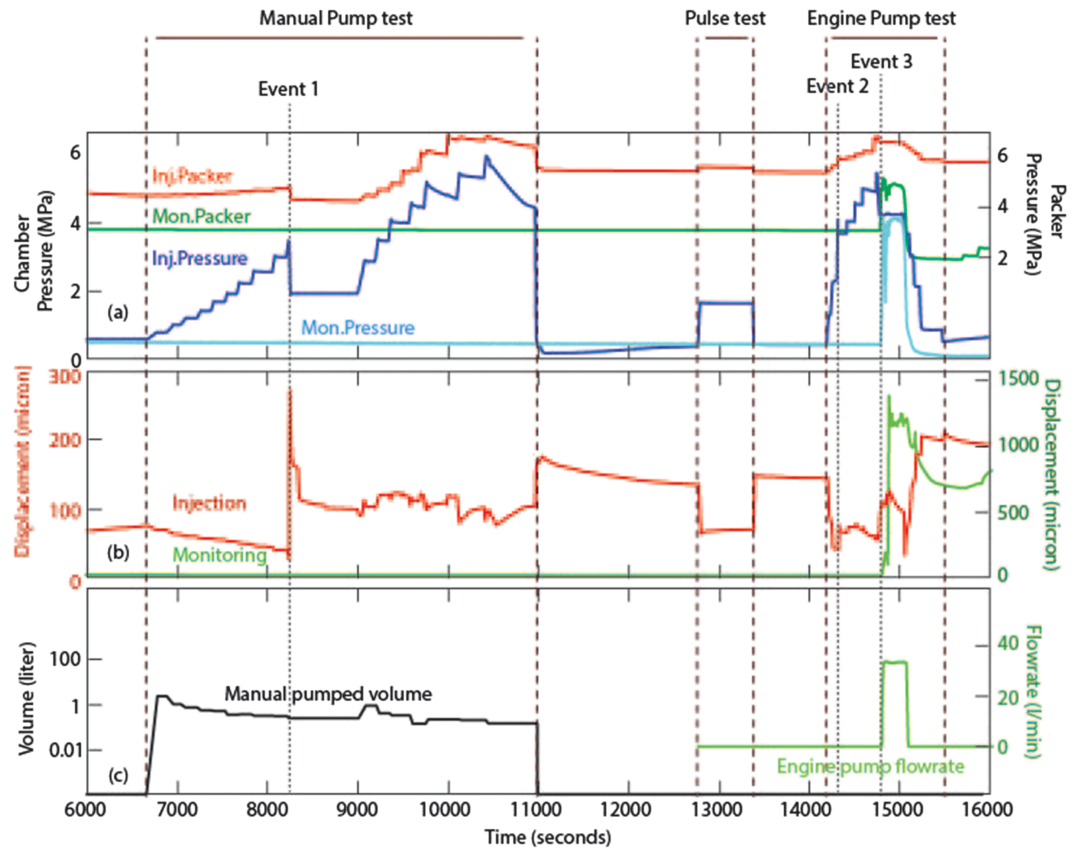


Figure 4. Time variations of (a) fluid pressure cycles (upper graphs), (b) norm of borehole displacements (middle graphs; the norm of displacement is not a directional feature. Thus, it is not having negative or positive trends.), and (c) injected volume and flow rate (lower graphs) during the Mont Terri fault activation experiment. The norm of displacement corresponds to the length of three-dimensional displacement vector calculated every 0.1 s. The green curve corresponds to the flowrate measured at the engine pump and the black curve to the volume of water injected during each pressure step of the manual pump test.

section of the borehole above the packer was sealed with resin. Pressure transducers were set at the borehole head and connected to the chamber with a 0.25-in. hydraulic line. Pore pressure was continuously monitored since the installation of the minipiezometers in April 2015, 6 months before the start of the

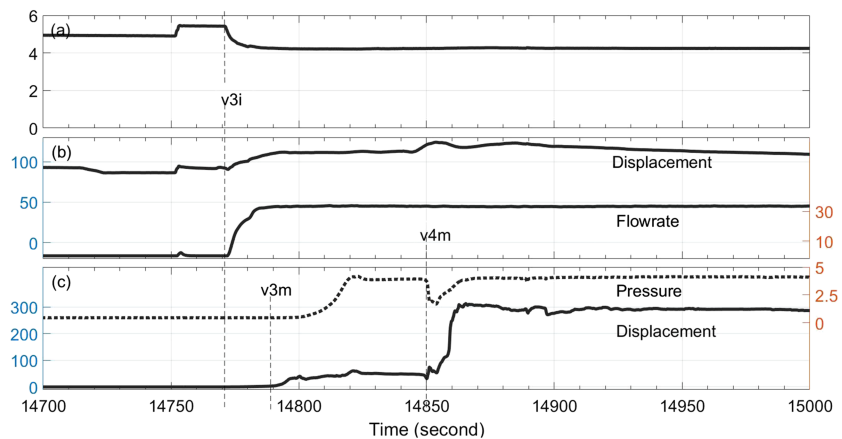


Figure 5. Time variation of injection pressure (a), injection hole norm of displacement and flowrate (b), and monitoring point pressure and norm of displacement during the fault rupture propagation conducted with the engine pump (c). The vectors \vec{v}_{3i} , \vec{v}_{3m} , and \vec{v}_{4m} correspond to displacement variations that initiate at both the injection (index *i*) and the monitoring boreholes (index *m*).

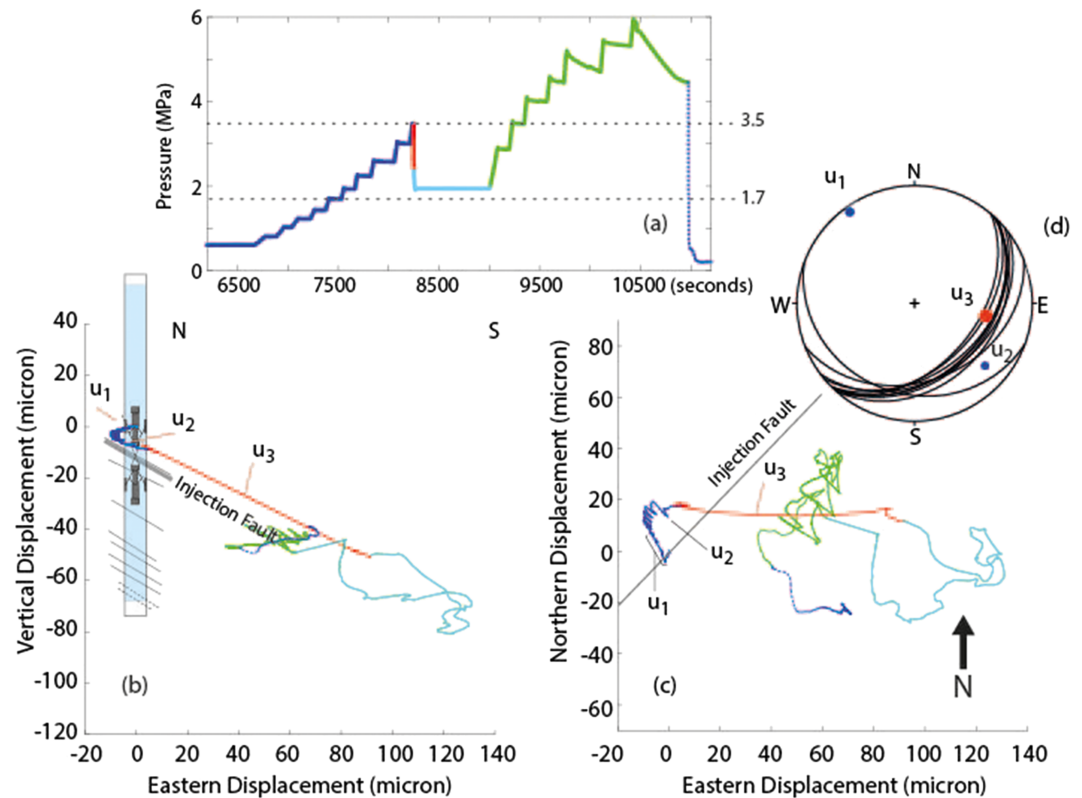


Figure 6. Fluid pressure and borehole displacements measured at the injection borehole during the fault rupture initiation cycle conducted with the manual pump (from 6,500 to 11,000 s in Figure 3). (a) Pressure variations. (b) Displacements variations in the vertical plane perpendicular to fault direction. (c) Displacements variations in the horizontal northeast plane (colored segments are the same on all graphs); (d) Stereographic lower hemisphere projection of fault planes affecting the interval and of vectors \vec{u}_1 to \vec{u}_3 describing the main displacement trends. The \vec{u}_3 appears to be located on the Injection Fault trace in Figure 5d. Dots for \vec{u}_1 to \vec{u}_3 represent the intersection of the displacement vector to the surface of the stereographic projection. The graphs show the displacements of the SIMFIP sensor upper anchor relatively to the lower anchor, which is considered fixed.

injection tests. About 2 months after installation, pore pressures stabilized at 0.9, 0.7, and 1.4 MPa respectively at BFS4, BFS5, and BFS6. Considering the accuracy of these measurements and in order to remain close to the lowest σ_3 value estimated by Martin and Lanyon (2003), the initial interval pressure before the injection tests was set at 0.6 MPa.

The two SIMFIP instruments were placed on the basis of core and image logs to attempt to isolate relevant fault features under the presumption they extended between the two boreholes. The borehole interval BFS-2 used for the injection tests is intersected by subparallel reactivated bedding surfaces in the fault damage zone (Figure 2). The displacement sensor was centered at 40.6 m depth, about 3.4 m above the Principal Shear Zone of the Main Fault (which is at 44.0 m depth in borehole BFS-2). The entire injection interval contains 13 subparallel fault planes striking N040°-to-N050° dipping 35°-to-55° SE, and one minor plane striking N110° dipping 24°SW, which is located at the bottom end of the interval where it is stopped by two N041° and N045° striking faults (see Figure 6d for stereographic projection of the planes intersecting the interval). The displacement sensor was anchored across the major fault plane identified within the injection interval at 40.6 m (Figure 2); as mentioned before, this plane is referred to as the Injection Fault in the remainder of the paper. It is a centimeter thick scaly clay layer with an average orientation of N042 to 36SE surrounded by four fault planes N035° to N050° with a dip angle of 32° to 40° SE. The clay, within the injection interval, is intact above the N042 to 36SE Injection Fault at 40.6 m (Figure 2).

In the BFS-1 monitoring hole, the test interval was set across a major slip surface (referred to as Principal Shear Zone or Monitoring Fault), which bounds the upper part of the Main Fault core and is locally

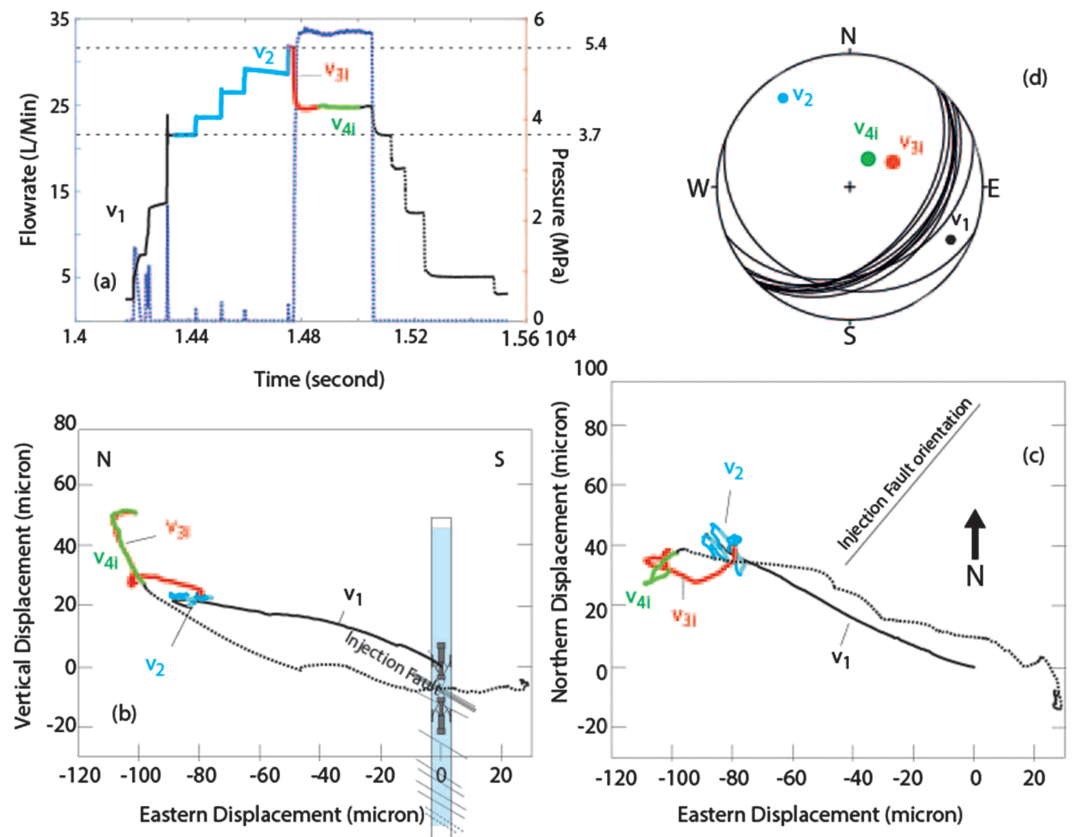


Figure 7. Fluid pressure and borehole displacements measured at the injection borehole during the fault rupture propagation cycle conducted with the engine pump (from 14,000 to 15,600 s in Figure 3). (a) Pressure variations. (b) Displacements variations in the vertical plane perpendicular to fault strike. (c) Displacements variations in the horizontal northeast plane (colored segments are the same on all graphs); (d) Stereographic lower hemisphere projection of fault planes affecting the interval and of vectors \vec{v}_1 , \vec{v}_2 and \vec{v}_{3i} describing the main displacement trends (no index and index i figure displacement vector at the injection borehole). Dots for \vec{v}_1 to \vec{v}_{3i} represent the intersection of the displacement vector to the surface of the stereographic projection.

oriented N050° and dipping 61°SE (Figure 2). The displacement sensor is anchored across this major N050° to 61°SE slip surface at 37.65 m (The surface of the principal shear zone is complex and picked as thick yellow sigmoids in Figure 2). Figure 8d shows the stereographic projection of all fault and fracture planes intersecting the monitoring interval. In addition to the principal shear zone, the entire monitoring interval contains two contrasted structural zones, the Main Fault core zone in the lower part, which contains several fault planes with fault gouge and three thick lenses of scaly clay, and a fractured damage zone in the upper part with a few fractures and a secondary fault oriented N120° dipping 25°SW with a thin scaly clay layer. The main (about 12 planes) discontinuity family is oriented N30-to-N60 dipping 55-to-75°SE (see Figure 8d).

3. Instruments and Experimental Protocols

3.1. The SIMFIP Borehole Instrument

The instrument used for the injection tests is a SIMFIP borehole probe, which allows simultaneous measurement of fluid pressure and three-dimensional displacements at high frequency (Guglielmi et al., 2014, 2015; Figure 3). The injection interval is isolated in an open hole using two inflatable rubber packers which are sliding sleeves straddled by a steel mandrel. The sealed interval is 2.4 m long. A 0.49 m long and 0.1-m diameter precalibrated aluminum cage located between the two packers is clamped on the borehole wall on both sides of an existing fault or fracture plane (Figure 3). When clamped, the cage is disconnected from the straddle packer system. As discontinuities intersected by the borehole interval are deforming as a

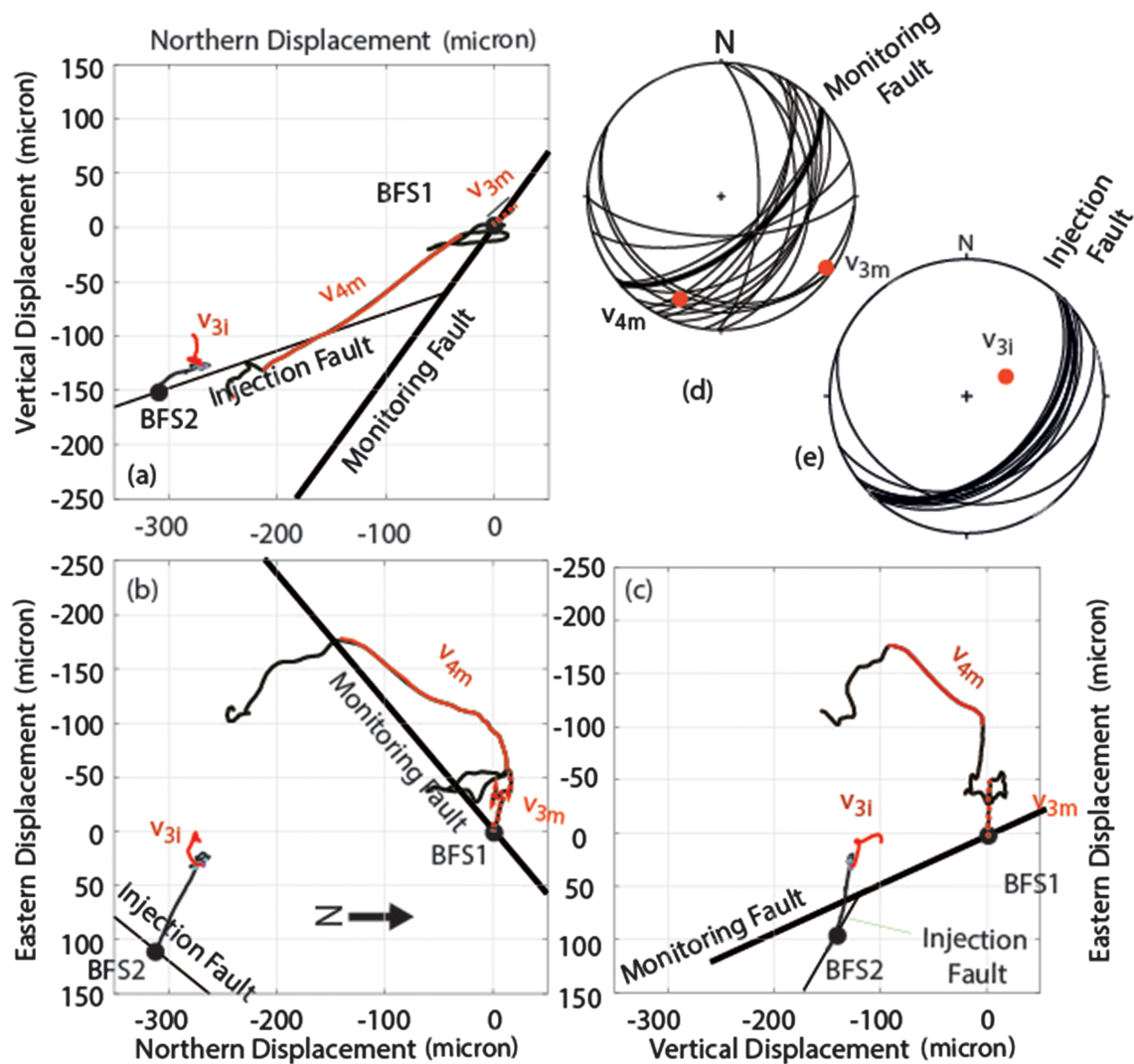


Figure 8. Displacement variations at both the injection and the monitoring points (a) in the vertical-north plane, (b) the east-north horizontal plane and (c) the vertical-east plane. Stereographs (d) and (e) show the vectors \vec{v}_{7i} to \vec{v}_{9m} , which correspond to displacements variations that initiate at both the injection (index i) and the monitoring boreholes (index m) during Events 3. Faults planes affecting the intervals are also plotted. In the stereographs, the injection and the monitoring faults are plotted as thick lines. Dots for \vec{v}_{7i} to \vec{v}_{9m} represent the intersection of the displacement vector to the surface of the stereographic projection.

result of the fluid injection into the interval, the cage allows obtaining angle dependent strain measurements which can be used to constrain the full three-dimensional displacement tensor and the three rotations of the upper anchor of the cage relatively to the lower anchor (see supporting information).

The maximum displacement range of the deformation cage is 0.7 and 3.5 mm in the axial and radial directions of the borehole, respectively, and the accuracy is $\pm 5 \times 10^{-6}$ m. A compass set on the probe provides the orientation of measurements with 0.1° accuracy. Thus, in further analyses, the displacements can be rotated into a geographic reference frame, for example, one where x is northward, y is westward, and z is vertical upward, or another where the displacement is expressed as opening and slip of the discontinuity.

The displacement data are continuously logged together with pump parameters (pressure and flow rate); oil pressure in the anchoring hydraulics and water pressure in the packer hydraulics (measured in the tunnel); as well as temperature and pressure in the borehole above, between and below the packers (the pressure and

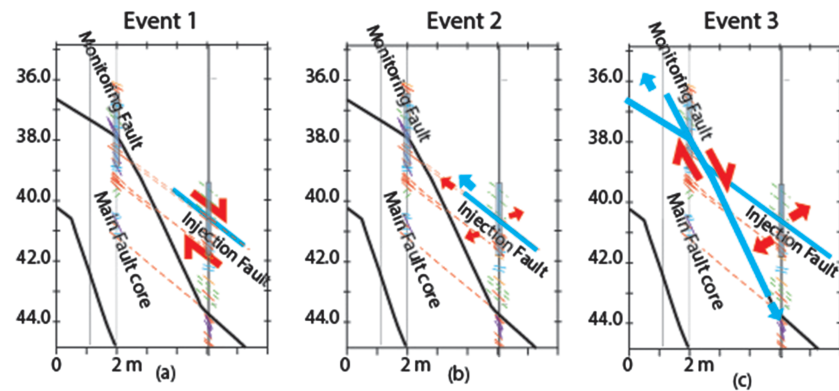


Figure 9. (a–c) Conceptual model of the fault activation sequence.

temperature sensors are set downhole). The pressure sensors allow for measurements over a pressure range from 0 to 10 MPa, with a 0.001 MPa accuracy. The accuracy of the temperature sensors is 0.1 °C.

The relation between the compliance of the probe and the elastic response of the borehole wall has been studied extensively through laboratory tests and fully coupled hydromechanical modeling using the TOUGH-FLAC simulator (Jeanne et al., 2017). It was shown that the device is ~10 times more compliant than the

rock, and that the orientation and magnitude of displacements below the stimulation pressure strongly depends on the elastic anisotropy of the rock. In the Mont Terri case, the SIMFIP response to the elasticity of the borehole wall is primarily related to the elastic anisotropy introduced by the bedding planes when few discontinuities are present in the measuring interval. This anisotropy is characterized by an elastic stiffness of the Opalinus Clay, which is 2.5 times higher parallel than normal to the bedding (Bock et al., 2010). The Young's modulus parallel to bedding is 10.0 GPa, and it is 4.0 GPa normal to bedding. In addition, the Poisson's coefficient is 1.4 times smaller parallel than normal to bedding, with values of 0.25 and 0.35 respectively. In theory, there should be no SIMFIP response for a uniform inflation of the pressurized interval in isotropic intact rock. In the Mont Terri case, the SIMFIP probe is capturing an elastic anisotropic response because the vertical interval is cross cutting the Opalinus Clay bedding planes which are striking N055°-to-N065° and dipping 50- to-55°SE. Typically, the SIMFIP displacement in response to this inclined elastic anisotropy of the interval is characterized by a N310°-to-N330° azimuth and 0-to-10°NW plunge and a 10-to-20 μm magnitude (see an example characterized by vector \vec{u}_1 in Figure 7 and Table 1).

During each injection test, the injection pressure is controlled by either a manual or an engine pump while flowrate, pressure, temperature, and displacement variations from the two SIMFIP probes, respectively, installed in the injection borehole and in the monitoring hole, are monitored with the same acquisition station. The sampling frequency is 500 Hz.

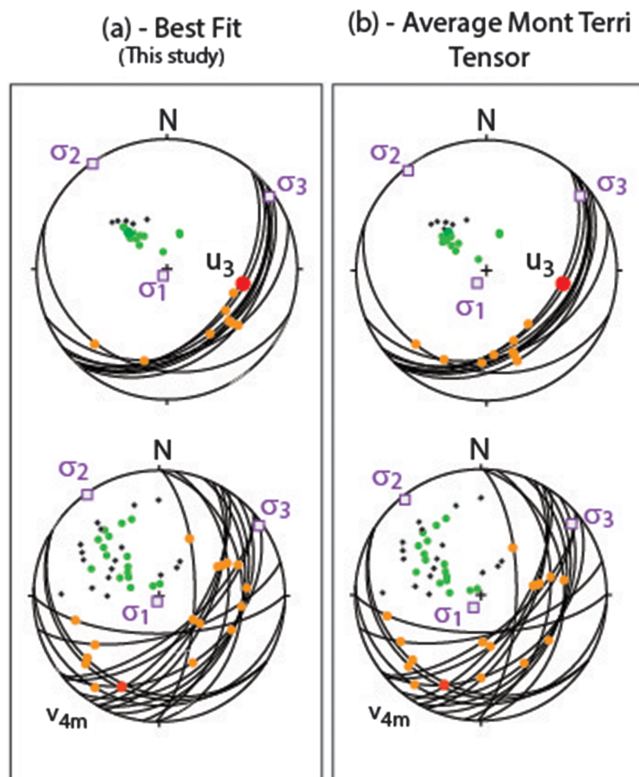


Figure 10. (a) Best fit stress tensor estimated by matching slip Event 1 with the maximum stress calculated on the Injection Fault. (b) Average Mont Terri tensor (see Table 2 for values). The stereographic projections show the principal stress orientations (purple squares), the measured fault displacements (red points), the calculated shear (orange points), and normal (green points) forces applied on the different fault planes affecting the injection (upper stereographs) and the monitoring point (lower stereographs). Black points are the poles of the planes.

3.2. Hydraulic Stimulation Protocol

The injection tests discussed in this study were conducted in Borehole BFS-2 (Figure 2, Injection hole), while Borehole BFS-1 interval was used for monitoring (Figure 2, Monitoring hole). When starting the fault stimulation, both boreholes remained in dry conditions. The monitoring probe was first set across the desired interval in the Monitoring Hole with the

Table 2
Stress Tensor at Mont Terri (upper lines) and Tensor Estimated in This Study (Lower Lines)

	Stress magnitude (MPa)	Dip direction	Dip
Mont Terri tensor (range of values from the bibliography)			
σ_1	6-to-7 (6.5)	210°	70°-to-90° (80°)
σ_2	4-to-5 (4.5)	310°	0°-to-7° (3.5°)
σ_3	0.6-to-2.9 (1.8)	52°	0°-to-18° (9°)
Tensor estimated in this study			
σ_1	6.2	210°	86°
σ_2	4.5	315°	0°
σ_3	2.0	55°	4°

Principal Shear Plane at its center. Packers were inflated to 1 MPa in order to seal the interval. Then, the displacement sensor was anchored to the borehole wall, and finally, the pressure in the monitoring chamber was set to 0.6 MPa in equilibrium with the formation pressure close to the fault. Following the monitoring probe installation, a similar procedure was followed to install the other probe in the Injection Hole. However, the packer pressure was then increased to about 3.5 MPa in the injection probe (during the subsequent testing, the packer pressure was increased again when the injection chamber pressure was increased in order to keep the differential pressure between packer pressure and chamber pressure to about 1.0 MPa). After installation and pressurization of both probes, a time delay of about 30 min was set for the

instruments to equilibrate toward pressure and temperature. The residual effect of the thermohydrromechanical equilibration between the probe-borehole system and the chamber's injected water, which is about 2 °C hotter than the borehole wall at the interval depth, explains the residual trend of the displacement baseline observed before the start of the injection test (see the norm of the displacement vector displayed in Figure 4b).

The total duration of the injection test was about 3 hr (from 6,000 to 16,000 s in Figure 4). The first injection into borehole BFS-2 was conducted with a manual pump (Figures 2 and 4a). Pressure was increased step-by-step by injecting limited volumes of water into the injection chamber (between 6,700 and 11,100 s in Figure 4c) at a very slow pressure increase rate of ~0.05 MPa/min (Figure 4a), to avoid any dependency of the hydromechanical response of the fault on the rate of pressurization (Haimson & Cornet, 2003). Each manual pump stroke was 1-s-long and corresponds to 15 ml of injected water. Pressure was increased by increments of 0.5 MPa. After each pressure step, the pumping was stopped for about 2 min. The total volume of pumped water was measured by weighting the manual pump tank and comparing this to the volume estimated from counting the pump strokes. By doing this, the accuracy of the manually pumped volume was about ± 1 ml. The total volume injected with the manual pump was about 0.69 L, after removing the compliance effects of the borehole interval and apparatus and assuming that water is incompressible. This phase allowed studying the initiation of the fault reactivation characterized by Event 1 at 8,245 s (Figure 4). The Event 1 rupture was limited to the nearfield of the injection borehole given the low amount of injected fluid. This was consistent with the fact that no pressure or displacement signal was observed at the monitoring hole located 3 m away horizontally.

At the end of the manual pump test (11,000 s in Figure 4), the injection chamber was opened until the chamber pressure stabilized back to the initial 0.6-MPa pressure. The flow back was not measured but a slight and progressive chamber pressure increase was observed between 11,000 and 12,700 s (i.e., some of the injected fluid may have flowed back into the chamber). When the chamber pressure had stabilized, a low-pressure Pulse Test was conducted (between 12,700 and 13,400 s in Figure 4) to estimate the hydromechanical response of the newly created rupture patch. Pressure was kept low to avoid any further rupture propagation (and the injected volume was not measured during the pulse).

Finally, between 14,100 and 15,500 s, a second pressure Step-Rate-Test was conducted with an engine pump, which can provide larger and more sustained injections than the manual pump. The intent of this second test was to propagate the rupture in the fault from the injection to the monitoring boreholes. Two rupture events (Events 2 and 3 in Figure 4a) were observed at 14,350 and 14,772 s, respectively, described in detail later in this paper. Event 2 was not clearly seen on the pressure curve but it appeared on the displacement curve at the injection point (Figure 4b). After Event 2, the pressure was increased further until a sudden pressure drop occurred in the injection hole corresponding to Event 3 (Figures 4a and 4b) followed 20 s later by a strong pressure signal in the monitoring hole, indicating a hydraulic connection had established (Figure 4c). This hydraulic connection was associated with a strong flowrate increase as the engine pump attempted to stabilize the pressure in the injection chamber (see expanded plot in Figure 5). This "step" was maintained longer than the previous steps in order to monitor the effects of continued fluid injection and propagation on the fault activation. Before a hydraulic connection was established (before Event 3), the measured flowrate was essentially zero. After Event 3, the

flowrate increased to about 33.5 L/s, and the total injected volume during this step (until 15,000 s) was about 143.1 liters. The second pressure test ended when between 15,000 and 15,500 s the fluid pressure was manually decreased step-by-step to its initial value. Again, most of the injected fluid stayed in the formation as no significant flow back was measured.

4. Experimental Results

4.1. Time Evolution of Pore Pressures and Fault Displacements

The data in Figure 4 show the complete test sequence including the manual and the engine pump cycles. No signal was measured at the monitoring well until 14,770 s when a hydraulic connection between the two boreholes occurred during the engine pump injection cycle. Thus, before 14,770 s, during the manual pump injection, the signals observed in the injection hole corresponded to “local” effects related to rupture initiation occurring in the near field of the injection well. At the end of the complete test sequence, “permanent” residual displacements of 200 and 813 μm remained at the injection and monitoring boreholes respectively, highlighting irreversible deformations.

During the manual pump test, there was an initial displacement decrease almost linearly varying with the step pressure increase in the injection chamber (Figure 4b). An abrupt displacement increase occurred at 8,245 s when injection pressure reached 3.45 MPa (Event 1 in Figure 4). Event 1 was quite short lasting only 2 s from 8,245 to 8,247 s. It was characterized by a 231 μm displacement event coinciding with a 1.6 MPa pressure drop. Following this first event, pressure could still be increased with the manual pump up to a maximum value of 5.95 MPa. During this period, the pressure did not stabilize during the pressure steps, indicating that there was some pressure leak-off into the formation corresponding to a cumulated 0.689-L leakage. Displacements displayed complex increasing and decreasing variations around an average value of 100 μm . At the end of the manual pump cycle (10,870 s in Figure 4), the opening of the pressure chamber induced an instantaneous ~ 60 - μm displacement increase followed by a slow decrease until quasi-stabilization at 14,200 s at the onset of the engine pump test. At this time, the residual displacement was 144 μm .

The pressure pulse conducted between 12,780 and 13,390 s at a low maximum pressure of 1.7 MPa allowed interpreting the quick bleed-off displacement as a reversible mechanical response of the borehole. The slow displacement decrease from the onset of the bleed-off at 10,870 to the onset of engine pump cycle at 14,200 s could be related to pore pressure readjustments in the rock adjacent to the borehole. Considering this slow pressure response of the chamber, we may postulate that the amplitude of displacement Event 1 could be explained by an irreversible borehole displacement of ~ 144 μm . The irreversible component of displacement could be caused by rupture growth away from the injection well, limited in size so that it does not propagate fully to the monitoring borehole. This is of course somewhat speculative since we do not have any monitoring points between the injection hole and the one monitoring hole about 3 m away.

The engine pump cycle showed five distinct periods, during which two main displacement Events 2 and 3 occurred (Figures 4b and 5):

1. From 14,200 to 14,322 s, there was a decrease of the displacement norm associated with the elastic response of the chamber to the pressure increase (Figure 4b; this decrease of the norm of displacement showed that borehole wall displacements were larger for pressure variations imposed during the initial low pressure steps compared to the high-pressure steps, highlighting a larger borehole expansion related to a restressing effect in the early steps. Overall, the borehole was expanding with pressure increase, but expanding more at the initial pressure increments.).
2. When pressure was increased from 2.35 to 4.1 MPa, there was an abrupt displacement increase of 34 μm (Event 2 in Figure 4b). Event 2 duration lasted 70 s from 14,350 to 14,420 s. It occurred at 3.69 MPa, which was close to the pressure value at which Event 1 occurred during the earlier manual pump cycle. No signals were observed in the monitoring hole.
3. From 14,420 to 14,770 s, there was a complex displacement behavior, while pressure was increased to a maximum value of 5.43 MPa. This period could be compared to the post-Event 1 period.
4. At 14,770 s, Event 3 occurred as a 45- μm displacement increase in the injection borehole and a 1.21-MPa pressure drop from 5.43 MPa associated with a large and rapid flow rate increase from 0 to 33.5 L/min.

The duration of Event 3 time was 24 s from 14,770 to 14,794 s (Figures 4b and 5). The \vec{v}_{3i} in Figure 5b shows the displacement vector during the duration of Event 3.

At the monitoring well, a displacement event was recorded about 8 s after the onset of Event 3 (\vec{v}_{3m} in Figure 5c). (Subscripts i and m refer to the injection and monitoring boreholes.) About 28 s after the onset of Event 3, a hydraulic connection was established between the injection and the monitoring holes that was characterized by a 4.17-MPa increase of the monitoring chamber pressure. Thus, the displacement event \vec{v}_{3m} in the monitoring chamber preceded the pressure increase in the monitoring chamber by about 20 s (Figure 5c). The following period displays a strong instability in pressure and displacements signals, which is observed in both boreholes (Figure 5). About 78 s after the onset of Event 3, a new event initiated at the monitoring point (\vec{v}_{4m} in Figure 5c), about 13 s long from 14,850 to 14,863 s. This occurred at 3.93 MPa and was associated with a 2.18 ± 0.01 -MPa pressure drop at the monitoring point (Figure 5c). In detail, this period was characterized by strong fluctuations in both displacement and pressure values.

4.2. Three-Dimensional Displacement Evolution

4.2.1. Rupture Initiation

During the manual pump test, four main displacement trends were successively observed corresponding to the different phases of rupture initiation (these phases are indicated as different colored graph segments in Figures 6a–6c):

1. The initial chamber response (dark blue segment from 6,206 to 8,245 s in Figure 6) at relatively low pressure (less than 1.7 MPa) was characterized by a N318° azimuth and 7°NW plunge displacement, which corresponds to vector \vec{u}_1 of 13- μm magnitude (Figures 6b–6d and Table 1). Above 1.7 MPa, displacements switched to a SE plunge. The largest of these SE plunging displacements occurred at 3.05 MPa. It corresponds to vector \vec{u}_2 from 8,086 to 8,211 s of 8- μm magnitude (Figure 6 and $\vec{u}_{2,4}$ in Table 1).
2. Event 1 as defined in Figure 4 initiated with a large, clear, and almost linear downward displacement toward the East, which corresponds to vector \vec{u}_3 (red segment in Figure 6). Vector \vec{u}_3 displays a N095° azimuth and a 26°E plunge. Displacement occurred from 8,245 to 8,247 s with a magnitude of 96 μm (Figure 6).
3. The post-Event 1 period (cyan segment from 8247 to 9003 s in Figure 6) displayed complex displacements trends. Displacement first continued downward, then was reversed upward with varying directions. The downward displacement was associated with most of the pressure drop, whereas there was almost no pressure variation during the upward period (Figure 6a).
4. When pressure was increased to the maximum of 5.95 MPa, there was an average NE-SW subhorizontal displacement trend, which was almost parallel to the injection fault direction (green segment from 9,003 to 10,970 s in Figure 6).
5. The final opening of the chamber (dashed blue segment starting at 10,970 s in Figure 6) showed a significant residual or permanent displacement related to Event 1 and to the NE-SW displacement reorientation at high pressure (Figures 6b and 6c).

The calculated azimuth, plunge, magnitude, starting, and ending time of the main displacement vectors \vec{u}_1 , \vec{u}_2 , and \vec{u}_3 are summarized in Table 1. The \vec{u}_3 is the largest magnitude displacement with the fastest displacement rate. We compared these vectors orientation with the orientation of the fault planes observed in the injection interval using a stereographic circle plot (Figure 6d). The \vec{u}_1 characterizes the initial reversible expansion of the injection chamber, which is preferentially oriented almost perpendicular to the N50° 35-to-45° dipping fault family affecting the chamber. Jeanne et al. (2017) showed that this \vec{u}_1 orientation and magnitude can be explained by the rock elastic modulus magnitude, which is 10 times lower perpendicular to existing fault planes than parallel to existing fault planes. The \vec{u}_2 and \vec{u}_3 plots on or close to the natural fault plane traces in Figure 6d. This means that these displacements are almost tangential to the preexisting natural planes. The \vec{u}_3 is consistent with irreversible shear along the N042 to 36°E Injection Fault plane located between the two SIMFIP anchors. It corresponds to a normal fault activation with a small right-lateral strike-slip component occurring at the injection pressure of 3.45 MPa. The \vec{u}_2 , which displays a roughly similar orientation but a much smaller magnitude than \vec{u}_3 , reveals that a smaller fault slip event might have initiated at lower injection pressures.

4.2.2. Rupture Propagation

During the engine pump test, several main displacement trends were successively observed corresponding to the different phases of rupture propagation. In Figures 7a–7c, these phases are indicated as different colored graph segments showing displacement behavior in the injection chamber:

1. The initial displacements in the injection chamber, from 14,204 to 14,322 s and up to a 2.41-MPa chamber pressure, were characterized by a N296° azimuth with an upward 13°NW plunge and a 102- μm magnitude (black segment in Figure 7 and vector \vec{v}_1 in Figure 7 and Table 1).
2. From 14,350 to 14,770 s, corresponding to pressure increases from 3.5 to 5.41 MPa (cyan segment in Figure 7), the azimuth of the displacement vector reversed to N135 to 168° with an upward 2° to 14° SE plunge. This occurred during the resting times between pressure steps and corresponded to small 5- to 14- μm magnitudes (vectors $\vec{v}_{2,1}$ to $\vec{v}_{2,4}$ in Table 1). We defined Event 2 in Figures 4 and 7 as the first reversed vector, which occurred from 14,350 to 14,420 s at 3.69 MPa ($\vec{v}_{2,1}$ in Table 1 also referred to as \vec{v}_2 in Figure 7). During this period, displacements remained relatively small, in particular when compared to \vec{v}_1 . Although the magnitudes were close to the accuracy limit of the measurements, the drastic change in the vector azimuth from N296° to N135° to N168° clearly indicated a change in the injection fault response to further pressure increases.
3. Event 3 was characterized by a complex displacement behavior from 14770 to 14,863 s during, which the injection pressure dropped strongly from 5.43 to 4.22 MPa (red segment in Figure 7). For the sake of simplicity, displacements in the injection borehole are described with one vector \vec{v}_{3i} , which is calculated based on the displacement coordinates at the beginning and at the end of Event 3 (Table 1). The \vec{v}_{3i} is characterized by a N251° azimuth with an upward 50°SW plunge and a 35- μm magnitude. In detail, complex direction changes in displacements occurred during this Event 3 period. The \vec{v}_{3i} displays a much larger dip than the previous vectors, highlighting a significant vertical opening of the injection fault.
4. After 14,863 s, displacements at the injection borehole displayed a N046° downward 57°NE plunge (green segment and \vec{v}_{4i} in Figure 7a and Table 1). The \vec{v}_{4i} corresponds to a partial closing of the injection fault, which followed the large displacement and the associated pressure drop that occurred from 14,850 to 14,863 s at the monitoring point (\vec{v}_{4m} in Figures 5 and 8 and Table 1).

Vector \vec{v}_1 shows a reverse shear along the N042 to 36°E Injection Fault plane (Figure 7d) triggered by the chamber expansion due to the initial pressure increase from 0.6 to 2.41 MPa. Such a large reversed shear was not observed during the manual pump test. We may speculate that it was favored by the earlier rupture of this plane during Event 1. The N153° azimuth of Vector \vec{v}_2 is almost perpendicular to the N042° azimuth of the injection fault (Figure 7d) and the 10° plunge of vector \vec{v}_2 has a $\sim 41^\circ$ angle with the dip of the fault plane. This displacement direction is consistent with the Injection Fault activation as a normal fault with shear and associated dilatant opening of the fault plane. Between Event 2 and the time when the pressure reaches 5.43 MPa, this activation remains limited and characterized by low magnitude displacement vectors (defined as $\vec{v}_{2,1}$ to $\vec{v}_{2,4}$ in Table 1). Finally when Event 3 occurs, the large change in both the azimuth and the plunge angle of vector \vec{v}_{3i} are difficult to explain by the activation of one single fracture direction. Rather this behavior reveals a complex hydraulic opening of the Injection Fault, which potentially involved the activation of several fractures of the injection interval (Figure 7d).

Figure 8 shows details of the three-dimensional displacement variations at both the injection (index i) and the monitoring boreholes (index m) including and immediately following Event 3 (red segment in Figures 4 and 7). Recall that this is the event during which both the displacement and pressure front propagate all the way from the Injection Hole to the Monitoring Hole. From 14,780 to 14,801 s, that is, 10 s after Event 3 initiated at the injection point and 20 s before the pressure increased at the monitoring point, the initial displacements at the monitoring point followed a N287° azimuth and 5° upward plunge (\vec{v}_{3m} in Figure 8 and Table 1). There was not much displacement variation during the pressure increase from 0.45 to 3.93 MPa at the monitoring point (see Figure 5 for details) until 14,850 s. From 14,850 to 14,863 s, a strong 228- μm magnitude event suddenly occurred, characterized by a N217° azimuth and 28° SW plunge (\vec{v}_{4m} in Figure 8 and Table 1).

The orientation of vector \vec{v}_{3m} is very different from \vec{v}_{4m} (Figure 8d). Since vector \vec{v}_{3m} corresponds to a displacement preceding the arrival of the pressure front at the monitoring point, its orientation may represent the

principal direction of deformation transferred by stress accumulation at the rupture front. In contrast, vector \vec{v}_{4m} is reasonably consistent with the activation of the N050° to 61°E Monitoring Fault as a normal fault with a right-lateral strike slip component (thick black line in the stereogram of Figure 8d).

5. Interpretation of Observations

5.1. Evidence of Opening and Slip During the Fault Activation

The test sequence highlighted a complex fault zone activation response characterized by a succession of rupture events observed in two boreholes about 3 m away in horizontal direction. There was an evolution of the measured displacements with regard to both the magnitude of the applied injection pressure and the temporal sequence of the injection test (Figure 9). During the first pressure cycle (manual pump cycle), rupture initiated at a pressure of 3.4- to 3.5 MPa applied in the injection borehole. It corresponded to a slip event occurring on the Injection Fault, which was activated as a normal fault (Event 1; Figure 9a). This event was associated to a 1.6-MPa pressure drop. Rupture Event 1 was limited in size since it was not detected at the monitoring hole. This first phase was followed by a period where the injection pressure was increased by a factor of about 1.6 without any significant fluid leakage into the fault zone. However, this corresponded to a large scattering of displacement directions, and it is difficult to relate these displacement orientations with the orientation of the natural fracture planes affecting the interval.

The second pressure cycle (engine pump cycle) showed that hydromechanical response of the Injection Fault after Event 1 was consistent with limited shear and associated dilatant opening of the fault plane. It also confirmed there was no significant fault leakage. During this second pressure cycle, Event 2 was triggered as a limited rupture event at about the same injection pressure as the earlier Event 1 during the first pressure cycle.

Upon further pressure increase to 5.43 MPa, there was a significant hydraulic opening of the Injection Fault characterized by the rapid flowrate increase from ~0 to 33.5 l/min. The observed Event 3 displayed a significant change in the displacement direction from tangential to the Injection Fault to about ~41° oblique, highlighting a dominant opening of the fault. This change evolved in complex dynamic patterns and in various directions illustrating that rupture propagated in a complicated manner through the multiple fractures of the injection interval. The fault rupture eventually propagated the few meters distance to the monitoring point where two main displacement signals were detected on the Monitoring Fault. The first displacement signal preceded by 20 s the hydraulic connection, which was characterized by a strong pressure increase. These displacements were interpreted as stress perturbations occurring at the rupture front propagating faster than the pressure front. The second displacement signal exhibited the largest displacements observed during the entire experiment, with an estimated slip magnitude of ~206 μm . These displacements were consistent with the activation of the N050° to 61°E Monitoring Fault as a normal fault with a right-lateral strike slip component. Associated to the slip-induced-normal-opening of ~71 μm , several pressure transients were recorded at the monitoring borehole (Figure 9c).

5.2. Relation Between the Measured Displacement Events and the Stress State at Mont Terri

In this section, we analyzed the influence of stress conditions on the average displacement trends observed in the experiments. To conduct this analysis, we used the stress tensor commonly adopted at the Mont Terri underground laboratory scale (Table 1) and entered it into the MohrPlotter open source software [R. W. Allmendinger©], which calculates the orientation and magnitude of the shear stress τ and normal stress σ_n on a single, planar discontinuity of given geometry. In the stereograms of Figure 10, the resulting τ and σ_n are respectively plotted as orange and green points for each of the fault planes intersected by the injection and the monitoring intervals. Assuming that the shear stress direction on any fault plane corresponds to the slip direction (Bott, 1959; Gephart, 1990; Wallace, 1951), we then varied the tensor orientation and magnitude until we got a reasonable match of the calculated shear stress orientation with the slip vector \vec{u}_3 measured on the Injection Fault during Event 1. This was done manually by trial and error and no uncertainty analysis was undertaken. The resulting stress tensor, which best explains the slip event measured during Event 1, could then be compared against the well-constrained Mont Terri stress tensor.

Figure 10 and Table 2 show that the tensor orientation and magnitude for which the calculated shear stress on the Injection Fault (red plane in Figure 10) best matches with the orientation of the slip vector \vec{u}_3 is in

reasonable agreement with the average Mont Terri tensor. Indeed, the maximum difference between our best fit tensor and the average orientation of the principal stresses is only 6° while our estimated magnitudes match the average values (Table 2). Using our best fit tensor direction and magnitude, we then calculated that the initial normal stress σ_n on the injection fault to be 5.5 ± 0.3 MPa. This is highlighting that, when Event 3 occurred at an injection pressure of 5.43 MPa, this pressure was sufficient to fully overcome the normal stress on the fault and thus to open the Injection Fault plane. In other words, the fault plane opened once the effective normal stress was sufficiently lowered.

In contrast, when using the same best fit tensor to compare the directions of the resolved shear stresses to the displacement vector \vec{v}_{4m} corresponding to the Monitoring Fault reactivation, we found that vector \vec{v}_{4m} orientation is poorly explained by this stress tensor. The reason for this discrepancy is not fully understood. We may postulate that either the local stress state on the Main Fault is different or that stress is not the only factor driving the reactivation of the Monitoring Fault.

5.3. Fault Displacements and Flow Transmission Through the Fault Zone

During Event 3, the Injection Fault opened and an increase in flowrate occurred at an injection pressure of 5.43 MPa. In contrast, no significant flow variation was seen during the first injection cycle when Event 1 occurred on the fault at 3.4 MPa nor during the second injection cycle when the smaller Event 2 occurred at 3.69 MPa. Thus, these earlier slip events did not seem to significantly unlock the fault and they failed to generate a leakage pathway. One reason could be that Event 1 generated a permeable path in the fault zone but this patch was of limited radius (since no signal was recorded at the Monitoring Hole 3 m away) and hydraulically confined. Event 2 was probably too small for the fault slip to propagate much. One simple explanation is that flow transmission through the fault zone between the two boreholes was observed only when the injection pressure got high enough to reduce the effective normal stress on the fault to about zero. This corresponds to an extreme pressurization of the fault, a likely necessary condition to grow the rupture in initially low permeability fault.

6. Discussion

Fault rupture and fluid leakages are documented in hydraulic injection operations in subsurface rocks. However, in situ studies aimed to identify fault activation and fluid flow mechanisms are rare, in particular, in very low permeability conditions. In this paper, the Mont Terri experiment provides valuable field scale insights into the role of stress in the injection-induced activation of an initially impermeable fault zone intersecting a clay formation. We find that the rupture initiation occurring near the injection borehole can reasonably be described by a conventional Coulomb stress criterion. Although the fault is unfavorably oriented with respect to the “regional” stress field, we conclude based on direct displacement measurements that fluid injection is producing a slip event at the fluid pressure source. This result is in good accordance with theoretical and crustal scale observations of high fluid pressures favoring the apparent weakness of faults unfavorably oriented toward stress (Axen, 1992; Faulkner & Rutter, 2001; Garagash & Germanovich, 2012; Rice, 1992). Nevertheless, we observe that rupture propagation is limited until the injection pressure is large enough to equal the normal stress on the fault(s) at the pressure source. This observation is in accordance with theoretical work showing that the local fluid pressure may have to reach the total normal stress on the fault before an eventual rapid rupture can be nucleated (Viesca & Rice, 2012).

We observe that dilation induced by sliding is not enough to generate fault permeability and leakage in this type of “closed” fault that has a very small permeability initially, close to that of the intact Opalinus Clay. Two mechanisms can explain why this mechanism is not enough. First, the complex channeling usually associated with dilatant slip may allow less fluid flow from an injection source point than the complete separation of the fault or fracture walls (Watanabe et al., 2008). Second, it has been observed in the laboratory that slip on rough fault surfaces can be associated with periods of dilation as well as with the progressive formation of gouge potentially leading to a permeability drop with cumulated shear (Faoro et al., 2009).

Thus it appears that a significant driving force is needed for fluids to flow into the fault, which would then increase the local pressure over a sufficiently large region, reduce the effective stress and trigger a large stress and strain perturbation at the tip of the overpressurized patch. Such dilatancy-assisted flow would allow

fluid to permeate along an initially “closed” fault and would finally pressurize a sufficiently large area to get shear. This behavior can only partially be explained by the orientation of fault structures toward stress. In addition, we suspect that the tortuous fluid propagation patterns expected in a complex fault zone is another key factor to consider when assessing fluid leakage in fault zones. Our direct field observations which couple local fault displacements with fluid pressure are in good agreement with laboratory tests, which show that for samples with low intact rock permeability and low fault permeability, excess fluid pressure is needed to significantly reduce the effective normal stress and trigger frictional sliding on a preexisting weak plane (Rutter & Hackston, 2017). In addition, Cuss et al. (2015) demonstrated in their laboratory studies that high-pressure migration of fluids into slipping clay-rich fault zones may generate preferential flow paths of small dimensions resulting in a complex spatial distribution of fluid pressure. Our field data show micrometer-scale variations in the displacement vectors with time, which suggests the development of complex preferential flow paths. We conclude that simple effective stress laws that consider a uniform pore pressure distribution in a fault of simple geometry is often not adequate for the prediction of fault reactivation in shale formations. This finding is consistent with Passelègue et al. (2018) who showed at laboratory scale that a nonlocal rupture initiation criterion should be considered to describe fault reactivation because of the fluid pressure heterogeneity within the fault.

Because we have two observations points with fluid pressure and mechanical displacement data in the rupture zone of the fault, we can evaluate dynamics of fluid and rupture propagation along the fault plane. We find that the largest rupture perturbation occurs after an overpressurized fault place in the damage zone connects with the principal shear zone of the Mont Terri Main Fault. In detail, the pressure source is located in a relatively less deformed zone, which is affected by secondary faults parallel to the Main Fault and almost perpendicular to the maximum horizontal stress. The injected fluids force their way along these initially low permeability planes of weakness (creation of new fractures could also occur given the uncertainty and the heterogeneity of the local stress state), creating large stress perturbations during the rupture growth in the fault zone. We observe that strain perturbation occurs ahead of the pressure perturbation and thus beyond the pressurized patch propagation. Our field observations are consistent with laboratory-scale observations from Rutter and Hackston (2017) who observed that overpressurized fluids suddenly entering a low-permeability fault zone after connection from a hydrofracture produced strong rupture instability characterized by stick-slip sliding. In addition, Cappa et al. (2018) showed through fully coupled hydromechanical modeling that the lower the initial fault permeability the larger is the stress and strain perturbation beyond the pressurized patch propagation.

Overall, we observe roughly 2.4 times smaller displacement magnitudes at the injection point compared to the monitoring point. It is not obvious that such contrasts can be explained by differences in the fault strength measured on laboratory-scale samples. Indeed, Thoeny (2014) conducted exhaustive shear tests in the laboratory on faults and reactivated bedding planes samples similar to the ones activated at the injection point and found a coefficient of friction of 0.19 to 0.4. These values are in the same range as the values of 0.31-to-0.37 obtained by Orellana et al. (2018) for saturated gouge samples from the principal shear zone instrumented at the monitoring point. Thus, at the laboratory scale the principal shear zone is not significantly weaker than the damage zone faults. However, its meter-scale roughness characterized by asperities mainly related to two directions (parallel to bedding and oblique to bedding), its kilometer size extent and the variability of stress levels may explain its overall larger weakness at the field scale. We speculate that the larger observed displacement at the monitoring point compared to the injection point caused by its smaller field-scale strength as has been suggested from observations on different faults zones (Fang & Dunham, 2013).

7. Conclusion

The field scale fault activation experiment conducted in the low-permeability Opalinus Clay in the Mont Terri Underground Research Laboratory (Switzerland) allowed the observation of fault rupture growth from a fluid injection point in the fault damage zone to a monitoring point within the fault core. Continuous measurements of downhole three-dimensional displacements coupled to fluid pressure changes were related to fault reactivation events and the potential for generating leakage pathways. We observed that significant pressure increases were required for the injected fluid to migrate through the initially almost

impermeable and mechanically weak fault planes connected to the injection source. Diffusion of injected fluid generated mixed mode rupture instability on the fault characterized by slip and opening of fractures associated with pressure transients. Our work suggests that the geometry of the fault zone is also a primary source of the rupture and flow complexity during fluid injection, which should be considered as a complementary mechanism to current models of rupture propagation and fluid pressure diffusion in faults.

This highly controlled and instrumented experiment showed details of the complex rupture processes related to high fluid pressures in a mature fault zone which are similar to those suggested from indirect observations on deep faults at reservoir and crustal scale. Our proposed explanation is that such dilatant deformation and channeling flow allow fluids to permeate along “closed” but heterogeneous fault zones, and finally pressurize a sufficiently area to get shear failure. Our observations have important implications about the way we typically evaluate fault reactivation, and how such activation may lead to loss of integrity of shale caprock and host rock barriers. Indeed, our experiments suggest that whatever its orientation toward the regional stress, a fault can become a leakage pathway even when displacements are very small as long as there is a large enough pressurized patch. Thus, given its practical implications, these results are of importance to better estimate the leakage potential of faults affecting low-permeability caprocks and highlight the need of investigating hydromechanical behavior of fault zone and local stress conditions at depth to characterize rupture and leakage mechanisms.

Finally, the injected volume in our experiments and the extent of the pressure perturbation were small compared to the size of the fault. Thus, upscaling these experimental results to larger scales is not a trivial challenge. On the other hand, although this is a field experiment, our in situ observations were made at a laboratory scale resolution. Thus, our observations may help to contribute to close the gap between laboratory scale and the tens-of-meter scales equivalent to fault rupture nucleation scales.

Acknowledgments

The authors are deeply grateful to the four partners of the Mont Terri Project that contributed to the funding of the FS experiment: the Swiss Federal Office of Topography (Swisstopo), the Swiss Federal Nuclear Safety Inspectorate (ENSI), the Japanese Atomic Energy Agency (JAEA), and the U.S. Department of Energy. The Mont Terri Project is an international research project for the hydrogeological, geochemical, and geotechnical characterizations of a clay formation (Opalinus Clay). Funding for Berkeley Lab's analysis of the FS data described in this study was provided by the Assistant Secretary for Fossil Energy as part of the Core Carbon Storage and Monitoring Research (CCSMR) and National Risk Assessment Partnership (NRAP) programs of the U.S. Department of Energy under Contract DEAC02-05CH11231. We thank the Editor, D. Schmitt, and the anonymous reviewers for insightful input that improved this paper. Experimental data are available in the supporting information.

References

- Amann, F., LeGonidec, Y., Senis, M., Gschwind, S., Wassermann, J., Nussbaum, C., & Sarout, J. (2018). Analysis of acoustic emissions recorded during a mine-by experiment in an underground research laboratory in clay shales. *International Journal of Rock Mechanics and Mining Sciences*, *106*, 51–59.
- Amann, F., Wild, K., Loew, S., Yong, S., Thoeny, R., & Franck, E. (2017). Geomechanical behaviour of Opalinus Clay at multiple scales: results from Mont Terri rock laboratory (Switzerland). *Swiss Journal of Geosciences*. <https://doi.org/10.1007/s00015-016-0245-0>
- Axen, G. J. (1992). Pore pressure, stress increase, and fault weakening in low-angle normal faulting. *Journal of Geophysical Research*, *97*(35), 8979–8991. <https://doi.org/10.1029/92JB00517>
- Barton, C. A., Zoback, M. D., & Moos, D. (1995). Fluid flow along potentially active faults in crystalline rock. *Geology*, *23*(8), 683–686.
- Barton, N., Bandis, S., Bakhtar, K. (1985). Strength, deformation and conductivity coupling of rock joints. *International Journal of Rock Mechanics and Mining Sciences and Geomechanics Abstracts*, Vol. 22, N° 3, 121 – 140.
- Bock, H., Dehandschutter, B., Martin, C. D., Mazurek, M., Haller, A. D., Skoczylas, F., Davy, C. (2010). Self-healing of fractures in argillaceous formations in the context of geological disposal of radioactive waste—Review and synthesis. OECD, NEA (N°6184).
- Bott, M. H. P. (1959). The mechanics of oblique slip faulting. *Geological Magazine*, *96*, 109–117.
- Cappa, F., Guglielmi, Y., Nussbaum, C., & Birkholzer, J. (2018). On the relationship between fault permeability increases, induced stress perturbation, and the growth of aseismic slip during fluid injection. *Geophysical Research Letters*, *45*, 11,012–11,020. <https://doi.org/10.1029/2018GL080233>
- Choi, J. H., Edwards, P., Ko, K., & Kim, Y. S. (2016). Definition and classification of fault damage zones: A review and a new methodological approach. *Earth-Science Reviews*, *152*, 70–87.
- Corkum, A. G., & Martin, C. D. (2007). Modelling a mine-by test at the Mont Terri rock laboratory, Switzerland. *International Journal of Rock Mechanics and Mining Sciences*, *44*, 846–859.
- Cuss, R. J., Harrington, J. F., Noy, D. J., Sathar, S., & Norris, S. (2015). An experimental study of the flow of gas along synthetic faults of varying orientation to the stress field: Implications for performance assessment of radioactive waste disposal. *Journal of Geophysical Research - Solid Earth*, *120*, 3932–3945. <https://doi.org/10.1002/2014JB011333>
- Doe, T., & Vietor, T. (2015). DS (Determination of stress) Experiment: Review of in situ stress measurements and their context. Synthesis report, Mont Terri Technical Report TR 2012-06. Federal Office of Topography (Swisstopo), Wabern, Switzerland. www.mont-terri.ch
- Ellsworth, W. (2013). Injection-induced earthquakes. *Science*, *341*.
- Evans, K. F. (2005). Permeability creation and damage due to massive fluid injections into granite at 3.5 km at Soultz: 2. Critical stress and fracture strength. *Journal of Geophysical Research*, *110*, B04204. <https://doi.org/10.1029/2004JB003169>
- Fang, Z., & Dunham, E. M. (2013). Additional shear resistance from fault roughness and stress levels on geometrically complex faults. *Journal of Geophysical Research - Solid Earth*, *118*, 3642–3654. <https://doi.org/10.1002/jgrb.50262>
- Faoro, I., Niemeijer, A., Marone, C., & Elsworth, D. (2009). Influence of shear and deviatoric stress on the evolution of permeability in fractured rock. *Journal of Geophysical Research*, *114*, B01201. <https://doi.org/10.1029/2007JB005372>
- Faulkner, D. R., Lewis, A. C., & Rutter, E. H. (2003). On the internal structure and mechanics of large strike-slip faults: Field observations from the Carboneras fault, southeastern Spain. *Tectonophysics*, *367*, 235–251.
- Faulkner, D. R., Mitchell, T. M., Healy, D., & Heap, M. J. (2006). Slip on “weak” faults by the rotation of regional stress in the fracture damage zone. *Nature*, *444*. <https://doi.org/10.1038/nature05353>
- Faulkner, D. R., & Rutter, E. H. (2001). Can the maintenance of overpressured fluids in large strike-slip fault zones explain their apparent weakness? *Geology*, *29*, 503–506. [https://doi.org/10.1130/0091-7613\(2001\)029<0503:CTMOOF>2.0.CO;2](https://doi.org/10.1130/0091-7613(2001)029<0503:CTMOOF>2.0.CO;2)

- Garagash, D. I., & Germanovich, L. N. (2012). Nucleation and arrest of dynamic slip on a pressurized fault. *Journal of Geophysical Research*, *117*, B10310. <https://doi.org/10.1029/2012JB009209>
- Gephart, W. J. (1990). Stress and the direction of slip on fault planes. *Tectonics*, *9*(4), 845–858.
- Goodman, H. E., Imbus, S. W., Espie, T., Minnig, C., Rösl, U., Fierz, T., & Lettry, Y. (2017). Large rock mass experimentation @ Mont Terri underground research laboratory—CO₂ containment assurance experiments. *Energy Procedia*, *114*, 5139–5150.
- Guglielmi, Y., Cappa, F., Lançon, H., Janowczyk, J. B., Rutqvist, J., Tsang, C. F., & Wang, J. S. Y. (2014). ISRM suggested method for step-rate injection method for fracture in-situ properties (SIMFIP): Using a 3-components borehole deformation sensor. *Rock Mechanics and Rock Engineering*, *47*(1), 303–311. <https://doi.org/10.1007/s00603-013-0517-1>
- Guglielmi, Y., Elsworth, D., Cappa, F., Henry, P., Gout, C., Dick, P., & Durand, J. (2015). In situ observations on the coupling between hydraulic diffusivity and displacements during fault reactivation in shales. *Journal of Geophysical Research: Solid Earth*, *120*, 7729–7748. <https://doi.org/10.1002/2015JB012158>
- Haimson, B. and Fairhurst, C. (1970). In-situ stress determination at great depth by means of hydraulic fracturing. *Rock Mechanics—Theory and Practice. The Proceedings of the 11th Symposium on Rock Mechanics*, 16-19 June 1969, Berkeley, 559-584.
- Haimson, B. C., & Cornet, F. H. (2003). ISRM suggested methods for rock stress estimation Part 3: Hydraulic fracturing (HF) and/or hydraulic testing of pre-existing fractures (HTPF). *International Journal of Rock Mechanics and Mining Sciences*, *40*, 1011–1020.
- Hearn, E. H., & Fialko, Y. (2009). Can compliant fault zones be used to measure absolute stresses in the upper crust? *Journal of Geophysical Research*, *114*, B04403. <https://doi.org/10.1029/2008JB005901>
- Jeanne, P., Guglielmi, Y., Rutqvist, J., Nussbaum, C., & Birkholzer, J. (2017). Field characterization of elastic properties across a fault zone reactivated by fluid injection. *Journal of Geophysical Research - Solid Earth*, *122*, 6583–6598. <https://doi.org/10.1002/2017JB014384>
- Jeanne, P., Guglielmi, Y., Rutqvist, J., Nussbaum, C., & Birkholzer, J. (2018). Permeability Variations Associated With Fault Reactivation in a Claystone Formation Investigated by Field Experiments and Numerical Simulations. *Journal of Geophysical Research - Solid Earth*, *123*, 1694–1710. <https://doi.org/10.1002/2017JB015149>
- Leclère, H., Cappa, F., Faulkner, D., Fabbri, O., Armitage, P., & Blake, O. (2015). Development and maintenance of fluid overpressures in crustal fault zones by elastic compaction and implications for earthquake swarms. *Journal of Geophysical Research: Solid Earth*, *120*, 4450–4473. <https://doi.org/10.1002/2014JB011759>
- Martin, C. D., & Lanyon, G. W. (2003). Measurement of in-situ stress in weak rocks at Mont Terri Rock Laboratory, Switzerland. *International Journal of Rock Mechanics and Mining Sciences*, *40*(7–8), 1077–1088.
- Matilla, J., & Tammisto, E. (2012). Stress-controlled fluid flow in fractures at the site of a potential nuclear waste repository, Finland. *Geology*, *40*(4), 299–302.
- Mitchell, T., & Faulkner, D. R. (2009). The nature and origin of off-fault damage surrounding strike-slip fault zones with a wide range of displacements: A field study from the Atacama fault system, northern Chile. *Journal of Structural Geology*, *31*, 802–816.
- Niu, F., Silver, P. G., Daley, T. M., Cheng, X., & Majer, E. L. (2008). Preseismic velocity changes observed from active source monitoring at the Parkfield SAFOD drill site. *Nature*, *454*. <https://doi.org/10.1038/nature07111>
- Nussbaum, C., Bossart, P., Amann, F., & Aubourg, C. (2011). Analysis of tectonic structures and excavation induced fractures in the Opalinus Clay, Mont Terri underground rock laboratory (Switzerland). *Swiss Journal of Geosciences*, *104*, 187–210.
- Olsson, R., & Barton, N. (2001). An improved model for hydromechanical coupling during shearing of rock joints. *International Journal of Rock Mechanics and Mining Sciences*, *38*, 317–329.
- Orellana, L. F., Scuderi, M. M., Collettini, C., & Violay, M. (2018). Frictional properties of Opalinus Clay: Implications for nuclear waste storage. *Journal of Geophysical Research: Solid Earth*, *123*, 157–175. <https://doi.org/10.1002/2017JB014931>
- Passelègue, F. X., Brantut, N., & Mitchell, T. M. (2018). Fault reactivation by fluid injection: Controls from stress state and injection rate. *Geophysical Research Letters*, *45*, 12,837–12,846. <https://doi.org/10.1029/2018GL080470>
- Raleigh, C. B., Healy, J. H., & Bredehoeft, J. D. (1976). An experiment in earthquake control at Rangely, Colorado. *Science*, *191*(4233), 1230–1237. <https://doi.org/10.1126/science.191.4233.1230>
- Rice, J. R. (1976). The localization of plastic deformation. In W. T. Koiter (Ed.), *Theoretical and Applied Mechanics* (pp. 207–220). Amsterdam: North-Holland Publishing Co.
- Rice, J. R. (1992). Fault stress states, pore pressure distributions, and the weakness of the San Andreas fault. In B. Evans, & T.-F. Wong (Eds.), *Fault mechanics and transport properties in rocks*, (pp. 475–503). London, UK: Academic Press.
- Rutter, E., & Hackston, A. (2017). On the effective stress law for rock-on-rock frictional sliding, and fault slip triggered by means of fluid injection. *Philosophical Transactions of the Royal Society A*, *375*, 20160001. <https://doi.org/10.1098/rsta.2016.0001>
- Savage, H. M., Kirkpatrick, J. D., Mori, J. J., Brodsky, E. E., Ellsworth, W. L., Carpenter, B. M., et al. (2017). Scientific exploration of induced seismicity and stress. *Scientific Drilling*, *23*, 57–63.
- Thoeny, R. (2014). Geomechanical analysis of excavation-induced rock mass behavior of faulted opalinus clay at the Mont Terri underground rock laboratory (Switzerland). Thesis, Engineering Geology Geological Institute ETH Zurich Sonneggstrasse 5 CH-8092 Zurich Switzerland, www.engineeringgeology.ethz.ch
- Thury, M., & Bossart, P. (1999). The Mont Terri rock laboratory, a new international research project in a Mesozoic shale formation, in Switzerland. *Engineering Geology*, *52*(3–4), 347–359.
- Townend, J., & Zoback, M. D. (2000). How faulting keeps the crust strong. *Geology*, *28*, 399–402.
- Viesca, R. C., & Rice, J. R. (2012). Nucleation of slip-weakening rupture instability in landslides by localized increase of pore pressure. *Journal of Geophysical Research*, *117*, B03104. <https://doi.org/10.1029/2011JB008866>
- Wallace, R. E. (1951). Geometry of shearing stress and relation to faulting. *Journal of Geology*, *59*, 118–130. <https://doi.org/10.1086/625831>
- Watanabe, N., Hirano, N., & Tsuchiya, N. (2008). Determination of aperture structure and fluid flow in a rock fracture by high-resolution numerical modeling on the basis of a flow-through experiment under confining pressure. *Water Resources Research*, *44*, W06412. <https://doi.org/10.1029/2006WR005411>
- Wiles, T. D., & Kaiser, P. K. (1994a). In-situ stress determination using the under-excavation technique—II. Application. *International of rock mechanics & geomechanics Abstracts*, *31*(5), 447–456.
- Wiles, T. D., & Kaiser, P. K. (1994b). In-situ stress determination using the under-excavation technique—I. Theory. *International Of Rock Mechanics & Geomechanics Abstracts*, *31*(5), 447–456.